Ultrafast Vibrational Relaxation Dynamics in XUV-Excited Polycyclic Aromatic Hydrocarbon Molecules

A. Boyer[1], M. Hervé[1], V. Despré[2], P. Castellanos Nash[3], V. Loriot[1], A. Marciniak[1],
A. G. G. M. Tielens[3], A. I. Kuleff[2,4] and F. Lépine[1]

[1]*Univ Lyon, Université Claude Bernard Lyon 1, CNRS, Institut Lumière Matière,
F-69622, Villeurbanne, France*
[2]*Theoretische Chemie, PCI, Universität Heidelberg,
Im Neuenheimer Feld 229, D-69120 Heidelberg, Germany*
[3]*Leiden Observatory, Leiden University, PO Box 9513, NL-2300RA Leiden, Netherlands*
[4]*ELI-ALPS, Wolfgang Sandner utca 3, H-6728 Szeged, Hungary*

Unraveling ultrafast molecular processes initiated by energetic radiation provides direct information on the chemical evolution under extreme conditions. A prominent example is interstellar media where complex molecules such as polycyclic aromatic hydrocarbons (PAHs) are excited by energetic photons. Until recently, ultrafast dynamics following such excitations remained largely unexplored due to the lack of relevant technologies. Here, we use time-resolved mass spectrometry combining ultrashort femtosecond XUV and IR pulses, to investigate the dynamics induced by high-energy photon excitation in PAHs. We demonstrate that excited cations relax through a progressive loss of vibrational selectivity, created at the early-stage dynamics, and which represents the first steps of a complete intramolecular vibrational energy redistribution. This process is in competition with the recently revealed correlation-band dynamics. These results might have direct consequences for the development of XUV molecular physics and other fields such as astrochemistry.

Subject Areas: Atomic and Molecular Physics

I. INTRODUCTION

Highly excited molecules are common species in the natural environment where irradiation occurs. Their dynamical properties are essential components of the nonstationary character of these media. Outer space is a prominent example where these species are encountered, especially in cold areas, such as diffuse molecular clouds, but also in hot areas of ionized matter. Surprisingly, in these areas, the molecular complexity is a sustainable property that has provided the richness and the variety of structures which allowed the appearance of complex biomolecules and eventually life in the Universe on astronomical timescale [1]. An important illustration of the quest for understanding molecular complexity in the Universe is the study of polycyclic aromatic hydrocarbon (PAH) molecules [2,3] that are suspected to represent about 15% of the carbon in the Universe and thus are strongly involved in the carbon chemistry of interstellar media.

In space, PAHs are exposed to XUV radiation, for instance, in protoplanetary disks or in the so-called photo-dissociation regions where XUV photons above 10 eV, emitted from the surrounding stars, can induce the fragmentation of structural changes of PAHs. Moreover, XUV photons can efficiently ionize PAHs and produce a number of photoelectrons that are responsible for heating processes of the molecular gas. Therefore, the importance of PAHs in interstellar media is determined by processes such as ionization, dissociation, and structural rearrangements that occur on ultrashort timescale, and that strongly influence parameters such as cloud temperature or molecular abundance [4–6]. Consequently, ultrafast XUV-induced dynamics is a cornerstone of astrochemistry modeling.

To understand the behavior of XUV-excited PAHs, laboratory experiments have been developed. Synchrotron facilities allow us to study the evolution of the photo-reactivity as a function of the photon energy [7]. This has shown that there exists a competition between ionization and statistical fragmentation, which strongly evolves with the molecular size. All these studies showed the complexity of the processes, including energy and size dependence. Unfortunately, the information on ultrafast properties of PAHs, ranging from attosecond to picosecond timescales, even at low excitation energy, remains scarce [8–12]. In this

context, time-resolved experiments require ultrashort pulses of energetic light in order to mimic the processes occurring in interstellar media. This has recently become accessible thanks to the development of tabletop high-order harmonic generation (HHG) sources. While several experiments have investigated ultrafast processes following XUV ionization in atoms and small molecules [13], it is only recently that these light sources have been applied to study ultrafast dynamics in larger systems [14–16]. The first ultrafast dynamics experiments in XUV-excited PAH was reported in Ref. [17] and showed the existence of unexpectedly long excited-state lifetimes for highly excited cationic states. It was followed by another experiment demonstrating that the relaxation timescale increases with the energy of the excited states [18]. Recently, we carried out studies on the dynamics of highly excited PAH cations and showed that these dynamics are driven by the presence of the so-called correlation bands (CBs) [19], which are features in the ionization spectra created by the electronic correlation [20]. So far, all these experiments have been conducted by monitoring the probe-induced ionization of the excited cation, thus probing the dynamics of electronic states just below the double-ionization threshold.

In this work, we investigate the dynamics of highly excited PAHs using XUV-IR pump-probe experiment, focusing on the time dependence of the fragmentation yield (time-resolved mass spectrometry). Our results show a simple general trend in which all fragmentation signals for a given molecule can be interpreted with only two timescales. We show that this trend is common to several PAHs and is directly linked to vibrational relaxation dynamics in the excited intact cation PAH, occurring after the relaxation of the CBs. Our results provide a general understanding of the XUV-induced ultrafast dynamics in PAHs, beyond each system's unique properties, and can serve in constructing models describing highly excited molecules.

II. EXPERIMENTAL SETUP

Our experimental setup was presented before (see Ref, [19]]; see Supplemental Material [21]). It is based on an amplified laser, delivering 25 fs near infrared pulses centered around 800 nm at 2 mJ per pulse with a repetition rate of 5 kHz. The near infrared beam is split in two parts using a 50:50 beam splitter to create a pump-probe interferometer. The first part is focused into a gas cell with a $f = 30$ cm lens to generate XUV photons through HHG in rare gas atoms. The XUV photon energy is controlled by changing the generation gas and covers a range from 20 to approximately 30 eV. The XUV beam is then reflected by a Nb_2O_5 mirror that removes the residual IR. The XUV beam is then reflected and focused on the molecular jet by using a toroidal mirror. An aluminum filter is inserted on the path of the XUV beam to remove the harmonics below the 11th order. The final XUV beam is used as the pump arm of the interferometer. The second

part of the IR beam passes through a half-wave plate and a polarizer to control the light intensity, then the IR beam is used as a probe and is delayed with a subfemtosecond precision using a delay line made of two wedges. The delayed beam is focused using a $f = 1$ m lens before being recombined with the XUV beam on a drilled mirror. The gas-phase molecules were injected using an oven filled with the corresponding molecule (in powder), and heated for sublimation of the sample to 90 °C (anthracene, $C_{14}H_{10}$), 120 °C (pyrene, $C_{16}H_{10}$), 210 °C (tetracene, $C_{18}H_{12}$), 240 °C (coronene, $C_{24}H_{12}$), 290 °C (pentacene, $C_{22}H_{14}$), and 450 °C [hexabenzocorone (HBC), $C_{42}H_{18}$]. The created molecular jet interacts with the XUV and IR pulses. The result of the interaction is then recorded with a time-of-flight (TOF) spectrometer. Delay-dependent TOF spectra were recorded using several XUV and IR conditions.

III. RESULTS

In the experiment, neutral molecules (PAHs) are photoionized by the XUV photons producing excited molecular cations with an internal energy that can reach more than 10 eV. The excited cations are then probed by a delayed IR pulse, leading to a second photoexcitation that can further ionize or fragment the charged molecule, if internal energy reaches the required threshold. The experiment consists of recording the variation of the fragments' yields as a function of the delay between the XUV pump and IR probe pulses. As explained below, this time-dependent signal carries information on the ultrafast dynamics in the excited cations following the XUV photoionization.

The mass spectrum resulting from the interaction of anthracene molecules ($m/q = 178$) with XUV light is shown in Fig. 1. In this case, high harmonics were generated in xenon and filtered with an aluminum filter which leads to an XUV bandwidth centered around 25 eV. The mass spectrum shows that the interaction with XUV light induces double ionization ($m/q = 89$), but also gives rise to a fragmentation pattern, corresponding to the loss of H_x and C_nH_x groups. This is a typical fragmentation pattern that is observed for all studied PAHs [22]. The same pattern is obtained when the XUV photon energy is changed to higher values using other rare gases as HHG targets. Only the relative intensity varies. These statistical fragmentation processes have been investigated in many experiments, showing that they occur after intramolecular vibrational redistribution (IVR) of the excitation energy, within the monocation [23]. To obtain the XUV-IR delay dependence of the fragments' yields, mass spectra were recorded at each pump-probe delay. The normalized two-color signal recorded for the doubly charged anthracene is shown in Fig. 1(c). It corresponds to the pump-probe signal from which we subtracted the background signal, and the signals obtained with IR only and XUV only. We observe a fast increase of the dication yield at the zero
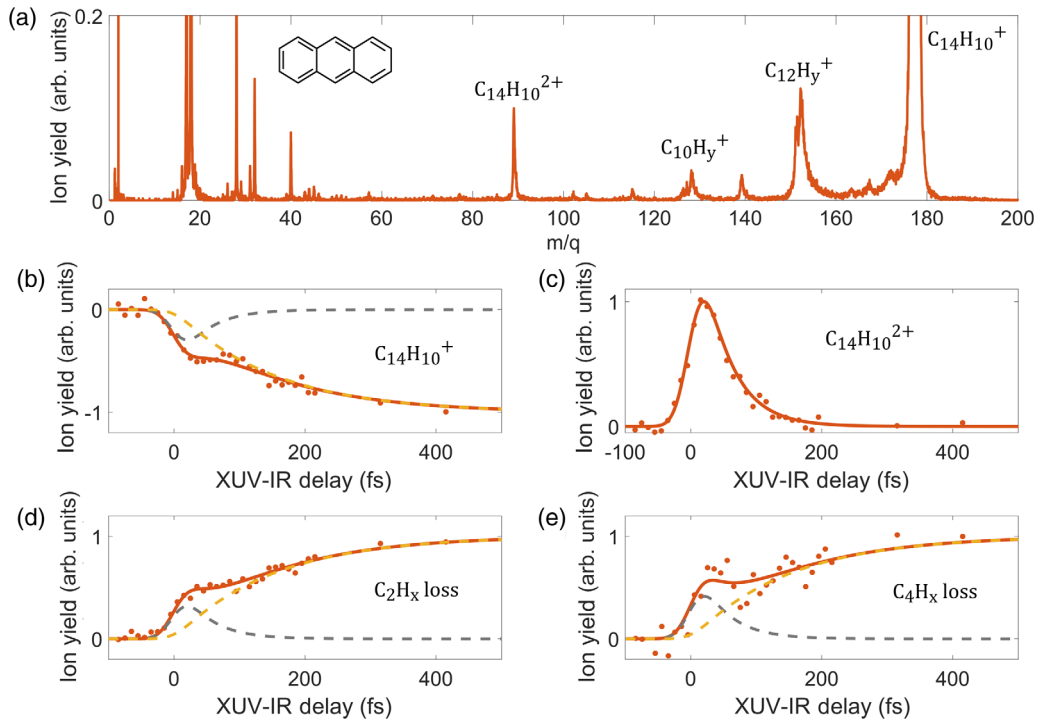
FIG. 1.   (a) Mass spectrum of anthracene after interaction with the XUV. (b) Cation yield as a function of the XUV-IR delay with a global fit (orange curve) and its breakdown in the two components: the exponential decay depletion (gray dashed line) and population (yellow dashed line). (c) Dication yield with exponential fit (d) C_2H_x loss yield as a function of the XUV-IR delay with a global fit (orange curve) and its breakdown in the two components: the exponential decay (yellow dashed line) and the increase exponential (purple dashed line). (e) Same as (d) but for loss of C_4H_x.

delay, where the two pulses overlap, followed by an exponential decay. The timescale of this decay is extracted through a standard fitting procedure using the convolution between the cross-correlation of the XUV and IR pulses and an exponential decay. Thus, we extract a decay (relaxation) time of $\tau_{\mathrm{decay}} = 37 \pm 6$ fs for anthracene.

Time-dependent signals are also observed for the yields of different fragments of anthracene. Here we consider the loss of C_nH_x groups. The pump-probe signal recorded for the loss of C_4H_x ($C_{10}H_y^+$) is shown in Fig. 1(e). A fast increase of the signal at zero delay is also observed, directly followed by a fast decay. However, after about 100 fs, the fragment yield starts growing again. Consequently, compared to the two-color signal obtained for the dication, the dynamics in the fragments can no longer be described by a single timescale but requires two time constants that we identify as a decay τ_{decay} and a population τ_{pop}. The same behavior is observed in the C_2H_x loss signal, although with different amplitudes for the two processes [see Fig. 1(d)]. By looking at the variations of other fragments' yields, corresponding to the loss of H, 2H, C_3H_x, C_5H_x, etc., (not shown here), we notice that the general trend is common to all the fragments.

The population time constant is then extracted through a fitting procedure using the following formula:

$$\Delta S(t) = \theta(t - t_0) \left\{ A_{\mathrm{decay}} \exp\left(-\frac{t - t_0}{\tau_{\mathrm{decay}}}\right) + A_{\mathrm{pop}} \left[1 - \exp\left(-\frac{t - t_0}{\tau_{\mathrm{pop}}}\right) \right] \right\}, \tag{1}$$

where τ_{decay} and A_{decay} are the time constant of the exponential decay dynamics and its amplitude, τ_{pop} and A_{pop} the time constant of the population dynamics and its amplitude, t_0 is the zero delay, and $\theta(t - t_0)$ is the Heaviside step function. We thus obtain a time constant of $\tau_{\mathrm{pop}} = 160 \pm 54$ fs for the population dynamics by fitting the signal of C_4H_x loss. A multidimensional fitting procedure is used to fit simultaneously the time-dependent yields of all fragments and dication with either independent or global parameters (see details in Appendix A1 and in the Supplemental Material [21]). Strikingly, this shows that time-dependent signals for all ions can satisfactorily be fitted with only two time constants, $\tau_{\mathrm{decay}} = 37 \pm 6$ fs, $\tau_{\mathrm{pop}} = 151 \pm 30$ fs. Therefore, we assume that the XUV dynamics observed in all these fragments correspond to essentially two processes. We also notice that τ_{decay} determines both the timescale extracted from the parent dication yield and the decay timescale observed in all the fragment signals.
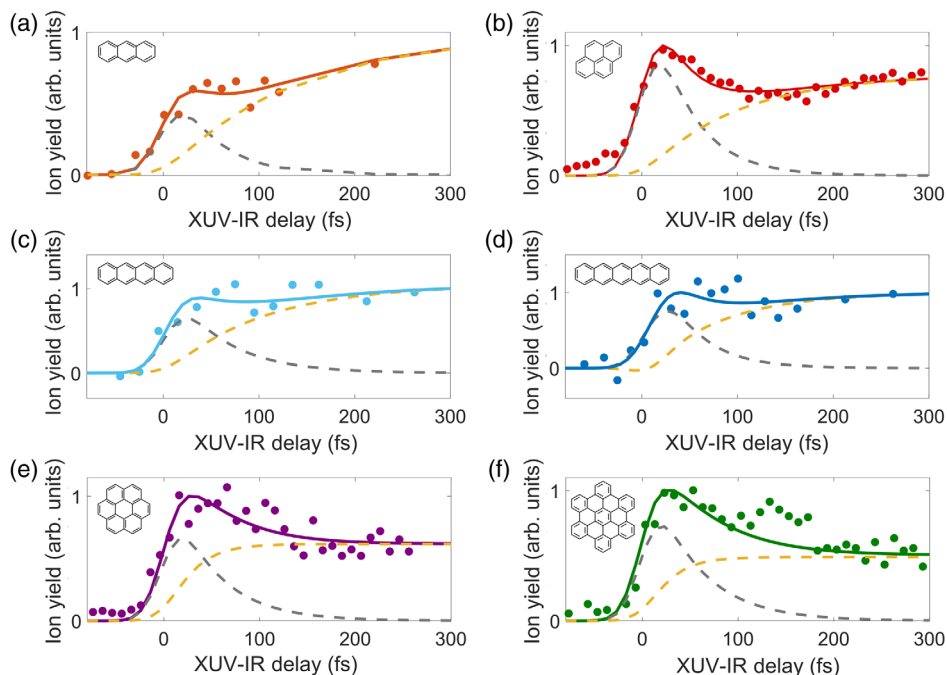
FIG. 2.   Fragmentation yield for the 2H-loss channel, as a function of the XUV-IR delay with a global fit and its breakdown into exponential decay (gray dashed curve) and population (yellow dashed curve) components, for six PAHs. (a) Anthracene in orange. (b) Pyrene in red. (c) Tetracene in sky blue. (d) Pentacene in blue. (e) Coronene in purple. (f) HBC in green. The color theme for the different PAHs is the same for the entire paper and the additional data shown in the Supplemental Material [21]. For the smallest PAH presented here, the abundance of other fragments contributes to the accurate determination of the timescales by using a multidimensional fitting procedure.

The same experiments have been performed for several PAHs from anthracene to HBC. Figure 2 presents the time-dependent signals obtained for the 2H loss in the case of six different PAHs (anthracene, pyrene, pentacene, tetracene, coronene, HBC). It shows that the trend described above is general to all studied PAHs. As expected, time-dependent signals are observed in the other fragments, corresponding to the loss of C_nH_x groups. However, these fragments are very weak for the largest PAHs and only 2H loss is considered in the following for the sake of comparison. We note, however, that the time-dependent signals recorded for all the fragments of a given molecule are always described by a decay timescale, similar to the one observed in the dication, and a population timescale. The two timescales have been extracted from the 2H-loss data for each studied PAH. For coronene and HBC, only a step appears in the time-dependent signals and no accurate population timescale could be obtained. Therefore, only the decay timescale could be extracted and an upper limit to the τ_{pop} is estimated. The evolution of the two timescales as a function of the number of valence electrons of the PAHs is shown in Fig. 3. We observe that the decay timescales increase with the number of valence electrons, a consequence of the dynamics in CBs, as demonstrated in Ref. [19]. On the contrary, the population timescales do not follow the same trend but decrease. Although the largest PAHs show an undefined timescale (see Supplemental Material [21]), it is clear that the

two timescales reach similar values above 100 valence electrons preventing the extraction of the timescale for larger systems.
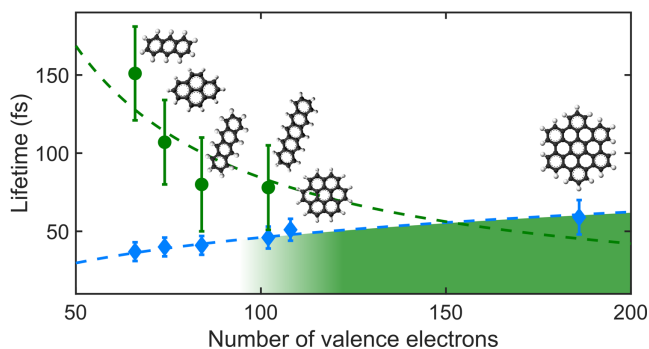

FIG. 3.   Extracted timescales for the nonadiabatic relaxation dynamics in the CB (blue diamonds) and the vibrational relaxation dynamics (green dots) as function of the size of the PAHs (anthracene to HBC) described by the number of valence electrons. We note that in the case of coronene and HBC, the experimental timescale of the vibrational relaxation dynamics is very inaccurate (shown by the shaded green area). The CB timescales are fitted using a logarithmic law and vibrational dynamics data are fitted with a $1/N$ law as discussed in the text. We note that the $1/N$ fitting is constrained in order to give only positive values to be consistent with our interpretation. The fitting curves are presented as blue and green dashed lines, respectively.

IV. DISCUSSION

In order to understand the general process observed in our experiment, we have to consider the first steps of the XUV photoexcitation, as well as the probing mechanism.

In the present situation, when the neutral PAH molecules are ionized by the XUV pump pulse, the produced cations are left in a large number of possible excited states. At high energy, the density of these states increases and new features are formed due to electron correlation. These features are named correlation bands [20] as they strongly resemble electronic bands in solid-state materials. After ionization, the energy deposited in these CBs relax through nonadiabatic effects, transferring the energy from the electronic to the nuclear degrees of freedom. This first step of the XUV-photoinduced dynamics corresponds to τ_{decay} and was studied in a series of PAHs measuring the time-dependent ionization (dication formation) yield (see Ref. [19]).

Here we use a different approach by considering not only the dication but the complete time-dependent fragmentation spectrum. Indeed, the photoexcitation by the IR probe pulse can not only lead to second ionization (forming a dication), but also to fragmentation of the cationic molecule, without ejection of a second electron. In order to understand the dynamics revealed by the time-dependent fragmentation yield, one needs to have a closer look at the probing process. The IR probing process is a transition between bound monocationic electronic states. The absorption probability of the probe pulse is determined by the overlap between the initial and final vibrational states involved in the transition [Franck-Condon (FC) overlap; see Supplemental Material [21]]. After IR absorption, internal vibrational redistribution occurs, eventually leading to high internal energy and statistical fragmentation [22,24,25]. The variation of the fragmentation yield as a function of the pump-probe delay is a signature of the variation of the IR absorption probability (i.e., variation of the FC overlap between vibrational states) occurring during the XUV-induced dynamics. In the case of highly excited states, where the density of states is high, we expect that there will always be an energetically accessible final state. Thus, the Franck-Condon overlap mainly depends on the localization of the vibrational wave function in the initial state. Therefore, the time-dependent signal can be interpreted in terms of vibrational dynamics, as described below.

During the CB relaxation the molecule evolves from highly excited electronic states to lower electronic states with higher vibrational energy (i.e., a spatially extended or "delocalized" vibrational wave function). This dynamic induces a decrease of the FC overlap that results in a decrease of the IR absorption probability and thus of the fragmentation yield. This is what is observed in Figs. 1(d) and 1(e), where τ_{decay} is measured in the C_2H_x and C_4H_x loss signals. We note that the relaxation in the CB favors the population of a subset of vibrational modes of the molecule

because the nonadiabatic relaxation occurs preferentially between states of similar symmetries. In our case, the dynamic is essentially driven by fully symmetric delocalized modes (see Ref. [18]).

Following this CB relaxation dynamic, the populated highly excited symmetric vibrational modes are then coupled to other modes, which leads to a progressive redistribution of the energy between all the vibrational degrees of freedom of the molecule. While the CB relaxation was characterized by a population of specific highly excited vibrational states, this second step corresponds to a population of various low excited vibrational states (i.e., a spatially confined or more "localized" vibrational wave functions). Therefore, this population transfer leads back to larger FC overlap and thus to a higher IR absorption probability. As a consequence, a progressive increase of the fragmentation signal is observed (see Supplemental Material [21] and Fig. 4) which corresponds to τ_{pop}. One might notice that this represents the first step toward a complete statistical exploration of the nuclear degrees of freedom corresponding to IVR.

As mentioned above, we observe that τ_{pop} decreases with PAH size. From the perspective of the vibrational relaxation dynamics described above, this evolution corresponds to the increasing number of accessible vibrational modes, among which the vibrational energy can be shared. This type of vibrational dynamics mechanism has been studied
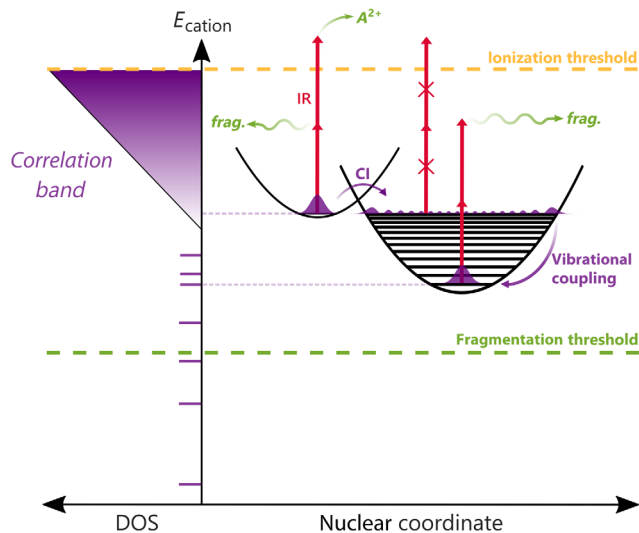

FIG. 4. Schematic of the IR probing of the two mechanisms in XUV ionized PAHs: CBs relaxation through conical intersections (CI) and nuclear relocalization due to vibrational coupling (vibrational dynamics). Both mechanisms are observed in the time-dependent fragmentation yield, as soon as the fragmentation threshold is overcome. The potential energy surfaces are schematically represented along one nuclear coordinate (right-hand part of the figure), while the density of states (DOS) populated by the XUV pulse is presented on the left-hand part.

in the context of laser-selective chemistry [26], where selective vibrational modes are excited in order to control the reactivity of a molecular system. In our case the relaxation in the CB can be seen as a way to prepare such a specific nuclear wave packet with only a limited subset of vibrational modes significantly excited. In this context, it has been shown that for complex molecules the coupling between the initially excited modes and the remaining ones can be modeled as coupling to a bath [19,27]. Using such a model, it is possible to derive a Fermi-golden-rule-like expression for the vibrational relaxation dynamics time-scale:

$$\frac{1}{\tau_{\text{pop}}} = \frac{2\pi}{\hbar}|V|^2\rho, \qquad (2)$$

where V is the average coupling between the initially excited modes and the remaining ones forming a bath, and ρ is the density of bath states. τ_{pop} evolves like the inverse of the density of bath states ρ, which is proportional to the number of vibrational modes and thus to the number of atoms n, $\tau_{\text{pop}} \propto (1/n)$. For the sake of a simpler comparison between τ_{pop} and τ_{decay}, it is useful to take advantage of the fact that the number of atoms n is proportional to the number of valence electrons N, $\tau_{\text{pop}} \propto (1/N)$ (for molecules with very different structure or chemical elements, the number of atoms n should be used). This behavior is validated by the good agreement with the fit in Fig. 3. This also implies that the coupling term V, which corresponds to the anharmonicity of the vibrational modes, weakly evolves between all the molecules studied here. This can be understood by the fact that V corresponds to a mean coupling with a finite set of vibrational states. In the complete IVR process, this coupling term would decrease with the size.

Overall, the timescales of the two mechanisms (CB relaxation and vibrational relaxation dynamics) have an opposite evolution with the PAH size. The larger the PAHs, the longer the population is trapped in the CBs following a logarithmic behavior (see Ref. [19]), while the vibrational relaxation dynamics is faster for larger molecules. The two processes reach similar timescales around $N = 100$. Interestingly, we note that this might impact the lifetime of any coherent process. XUV-induced electronic and vibrational coherence is a subject of great interest in current ultrafast science, which has motivated experimental and theoretical investigations [28]. In such investigation, the coherence loss is defined as the disappearance of dynamics corresponding to a photoinduced time-dependent coherent wave packet. The vibrational relaxation dynamics is a first step toward such coherence loss because the phase will spread over a large number of degrees of freedom and will never be recovered. According to our measurements, in small PAHs, the population stays longer in specific vibrational modes; therefore the coherence in the CB could be maintained until vibrational energy redistribution occurs.

Thus, we expect that for highly excited molecules, the coherence would quickly disappear after the relaxation of the CBs due to the vibrational relaxation dynamics followed by complete IVR. This should be the case for large PAHs for which τ_{pop} is faster than τ_{decay}. However, for smaller PAHs, after the relaxation in the CBs, the wave packet is trapped for some time in the lower electronic states before going through an IVR. For instance, coherence can be maintained longer than 30 fs in highly excited anthracene, because of the 100 fs vibrational dynamics. This observation could explain recent results on vibrational coherence observed in small PAHs [18], and similar implications concern electronic coherence [29]. Obviously, the complex electronic structure of CB implies that the design of a time-dependent wave packet with a broadband laser pulse is highly nontrivial and needs to be investigated.

V. CONCLUSION

In this work, we performed XUV-IR pump-probe experiment on a series of PAHs, to investigate the dynamics of XUV-induced excited states. In contrast with previously reported experiments, this work analyzes the time-dependent fragmentation yield. Surprisingly, we found that for a given molecule, the time-dependent signals of all fragments are described by only two time constants. The first one corresponds to the relaxation in the correlation bands, reported in a previous experiment on time-resolved photoionization [19,20]. The second one brings new information about the energy sharing pathways in highly excited PAHs involving vibrational relaxation dynamics. Indeed, the CB relaxation preferentially populates highly symmetric vibrational modes, in highly excited, "delocalized" vibrational states. In a second step, vibrational couplings to other vibrational degrees of freedom lead to excitation of other, weakly excited modes (more "localized" vibrational wave functions). This transition between highly excited few vibrational modes to weakly excited multiple vibrational modes represents the onset of the process of IVR. By measuring the size dependence of both timescales, we deduce that the two processes converge toward similar timescales for molecules with around 100 valence electrons. This might have an influence on how the coherence and excitation is managed by the molecule. These observations bring new opportunities on the control of coherence in highly excited molecules and might contribute to explain the existence of long-lived electronic and vibrational coherences, over several tens of femtoseconds, in molecules of similar sizes. Ultrafast dynamics induced by XUV excitation in PAH is barely studied; this work focused on the internal energy dynamics of highly excited PAH cations. The fragmentation dynamics itself could also be studied in a time-resolved fashion, providing a direct examination of the reaction pathways that are very complex in PAH-like molecules [30]. Overall, accurate dynamical information

on XUV excited PAH might serve in improving astrochemistry models.

All relevant data supporting the key findings of this study are available within the article, in the Supplemental Material [21], or from the corresponding authors upon reasonable request.

APPENDIX A: METHODS

1. Data analysis

In order to extract the population time constant shown in Fig. 3, several steps of analysis were performed. In each step, the following formula was used to fit the experimental data:

$$
\begin{aligned}
S_{\text{fit}}(t) = \exp&\left[-4\ln(2)\left(\frac{t}{\tau_{Xco}}\right)^2\right] \\
&\times \otimes \left(\theta(t-t_0)\left\{A_{\text{decay}}\exp\left(-\frac{t-t_0}{\tau_{\text{decay}}}\right)\right.\right. \\
&\left.\left. + A_{\text{pop}}\left[1-\exp\left(-\frac{t-t_0}{\tau_{\text{pop}}}\right)\right]\right\}\right),
\end{aligned}
\tag{A1}
$$

where τ_{Xco} and t_0 are fixed parameters.

The first step in the analysis assumed A_{decay}, A_{pop}, τ_{decay}, and τ_{pop} as independent parameters for every fragment. From this first step, we noticed that the decay timescales obtained in fragmentation signals seem to be the same as the decay timescale extracted from the dication signal, within the error bar. Thus, we assumed that this timescale should also be visible through the fragmentation signals and should be similar.

Therefore, the second step of the analysis consisted in constraining the fitting procedure by using the decay timescale extracted from the dication signal as a fixed parameter. The parameters A_{decay}, A_{pop}, and τ_{pop} were considered as independent from one fragment to another. Some results obtained in different fragments for all the studied PAHs are given in the Table S1 of the Supplemental Material [21], showing that the obtained values for τ_{pop} are similar from one fragment to another, within the error bar.

Thus, in order to improve our estimation of τ_{pop}, we constrained the fitting by forcing τ_{pop} to be common to all the fitted fragments. The results of this last step of analysis are plotted in Fig. 3. The numerical value of some of the extracted timescales are given in the Table S1 of the Supplemental Material [21] (All Fragments). The time-dependent signals and corresponding fitting are shown in Figs. 1 and 2. More data are also available for pyrene, tetracene, and pentacene in the Fig. S2 of the Supplemental Material [21]. The fitting curves, using a common τ_{pop}, are in good agreement with the experimental data.

2. Theoretical methods

The ionization spectra of naphtalene, anthracene, and pyrene have been obtained using third-order non-Dyson algebraic diagrammatic construction methodology [nd-ADC (3)], with cc-pVDZ basis set. This level of theory allows us to include two-holes one-particle configurations. From the ADC calculations, we could extract the corresponding density of states (DOS), showing that below the second ionization potential (at the energy range of the CBs) the DOS increases linearly with the energy. Regarding this high DOS, we developed a model based on an analogy with solid-state physics that has been explained in detail in our previous paper (see Ref. [19]). This model describes the relaxation of the CBs as electron-phonon scattering. Assuming that, we were able to derive a simple relation between the relaxation of the correlation bands τ and the number of valence electrons N:

$$
\tau = \tau_0 \, \ln \frac{N}{N_{\text{CB}}},
\tag{A2}
$$

where τ_0 is the mean lifetime of an excited electron inside the CBs and N_{CB} corresponds to the lower limit of validity of the above formula. This law describes the evolution of the decay dynamics τ_{decay} observed in this paper by looking at the fragmentation yield. It is represented in Fig. 3 by a blue dashed curve.

After the relaxation of the CBs, vibrational modes are populated. To decipher which vibrational modes are involved in the relaxation of the CBs, we have performed propagation calculations describing the dynamics triggered by ionization in the case of naphthalene using multiconfiguration time dependent Hartree calculations (more details about these calculations can be obtained if Ref. [18]). Thus, we could extract the nonadiabatic dynamics taking place between the molecular electronic states, showing that the totally symmetric modes (of a_g symmetry) are the modes with the most efficient coupling.

The calculations could only be performed on naphthalene, but the coupling with totally symmetric modes should also be the most efficient for larger PAHs, such as the ones presented in this paper. Indeed, electron correlation creates a large number of states with the same symmetry after the removal of an inner-valence shell electron. These states are then coupled by symmetric normal modes due to selection

rules, meaning that totally symmetric modes are the last step of the relaxation of the CBs, thus the first step of the subsequent dynamics.

Therefore, the vibrational relaxation process represents the redistribution of the vibrational energy deposited in a small subset of totally symmetric vibrational modes to the remaining accessible modes of the system. This energy redistribution from a few states to a large number of modes (bath) is governed by the intermode coupling V in the system. The probability for such an energy dissipation can be calculated by Fermi's golden rule, giving the transition probability per unit time Γ from an initial state $|\psi_\nu\rangle$ to a set of final states $|\psi_{\nu'}\rangle$,

$$\Gamma_{\nu \to \nu'} = \frac{2\pi}{\hbar} |\langle \psi_{\nu'}|V|\psi_\nu \rangle|^2 \rho(E_{\nu'}), \qquad \text{(A3)}$$

where $\rho(E_{\nu'})$ is the density of final states. The relaxation time τ_{pop} is, therefore, given by the inverse of $\Gamma_{\nu \to \nu''}$; that is

$$\tau_{\text{pop}} = \frac{\hbar}{2\pi|V|^2} \frac{1}{\rho(E_{\nu'})}. \qquad \text{(A4)}$$

Because of the similarity in the structure and symmetry of the different PAH molecules, the averaged intermode coupling is expected to vary only very weakly among the different members of the PAH family. The vibrational relaxation time, therefore, will decrease with the increase of the density of final states (modes) ρ. As the number of modes increases linearly with the number of atoms in the molecules, the density of states will be proportional to the number of atoms n in a given PAH. We can also use the fact that the PAHs are constructed of only two types of atoms and, therefore, relate the number of atoms in the molecule with the number of valence electrons N. We, therefore, can see that the vibrational relaxation time is inversely proportional to the number of valance electrons:

$$\tau_{\text{pop}} = \text{const} \frac{1}{N}. \qquad \text{(A5)}$$

This trend is indeed observed in our experimental data. Thus, it confirms our understanding of the population dynamics as a redistribution of energy through vibrational coupling.

APPENDIX B: ADDITIONAL RESULTS ON STATISTICAL FRAGMENTATION

In this paper, we focus on the fragmentation yields of different PAHs. In order to understand the nature of this fragmentation, we measured the fragment ion kinetic energy distribution.

Using gated detection, we were able to select a particular $m = q$ fragment ion of interest and perform momentum measurements by using a velocity map imaging (VMI)
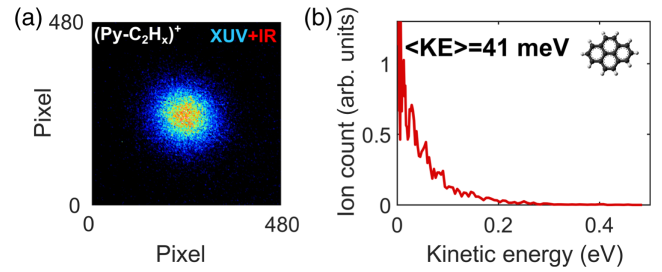

FIG. 5. Velocity map imaging measurements performed on pyrene. (a) Raw VMI image of C_2H_X loss in pyrene and (b) corresponding kinetic energy distribution of $(Py\text{-}C_2H_x)^+$ ions.

spectrometer based on the design by Eppink and Parker [31]. A raw VMI image (in pixel) corresponding to the ions $(Py\text{-}C_2H_x)^+$ is shown in Fig. 5(a). By performing Abel transform, we could then obtain the velocity distribution of the different fragment ions emitted after the absorption of XUV and IR pulses. After calibration, we could also extract the corresponding kinetic energy distribution [an example for $(Py\text{-}C_2H_x)^+$ is shown in Fig. 5(b)]. We observe that the velocity distribution is isotropic with a low energy distribution with a mean value of few tens of meV. This is clearly the signature of statistical fragmentation. Similar values of few tens of meV were obtained in other fragments. This supports the description of the probing mechanism as a bound-bound IR transition leading to statistical fragmentation after IVR. This also confirms our interpretation of τ_{pop} as a general process occurring in the excited cation, as discussed in the main paper and Appendix A.

[1] A. G. G. M. Tielens, *The Molecular Universe*, Rev. Mod. Phys. **85**, 1021 (2013).

[2] L. J. Allamandola, A. G. G. M. Tielens, and J. R. Barker, *Polycyclic Aromatic Hydrocarbons and the Unidentified Infrared Emission Bands: Auto Exhaust along the Milky Way*, Astrophys. J. **290**, L25 (1985).

[3] A. Leger and J. L. Puget, *Identification of the "Unidentified" IR Emission Features of Interstellar Dust?*, Astron. Astrophys. **137**, L5 (1984).

[4] E. L. O. Bakes and A. G. G. M. Tielens, *The Photoelectric Heating Mechanism for Very Small Graphitic Grains and Polycyclic Aromatic Hydrocarbons*, Astrophys. J. **427**, 822 (1994).

[5] R. Visser, V. C. Geers, C. P. Dullemond, J.-C. Augereau, K. M. Pontoppidan, and E. F. van Dishoeck, *PAH Chemistry and IR Emission from Circumstellar Disks*, Astron. Astrophys. **466**, 229 (2007).

[6] E. R. Micelotta, A. P. Jones, and A. G. G. M. Tielens, *Polycyclic Aromatic Hydrocarbon Processing in Interstellar Shocks*, Astron. Astrophys. **510**, A36 (2010).

[7] S. Lepp, A. Dalgarno, E. F. van Dishoeck, and J. H. Black, *Large Molecule in Diffuse Interstellar Clouds*, Astrophys. J. **329**, 418 (1988).

[8] J. Zhen, S. R. Castillo, C. Joblin, G. Mulas, H. Sabbah, A. Giuliani, L. Nahon, S. Martin, J.-P. Champeaux, and

P. M. Mayer, *VUV Photo-Processing of PAH Cations: Quantitative Study on the Ionization versus Fragmentation Process*, Astrophys. J. **822**, 113 (2016).

[9] W. R. Lambert, P. M. Felker, and A. H. Zewail, *Jet Spectroscopy of Anthracene and Deuterated Anthracenes*, J. Chem. Phys. **81**, 2209 (1984).

[10] W. R. Lambert, P. M. Felker, and A. H. Zewail, *Dynamics of Intramolecular Vibrational-Energy Redistribution (IVR). II. Excess Energy Dependence*, J. Chem. Phys. **81**, 2217 (1984).

[11] M. H. Stockett, H. Zettergren, L. Adoui, J. D. Alexander, U. Bērziņš, T. Chen, M. Gatchell, N. Haag, B. A. Huber, P. Hvelplund, A. Johansson, H. A. B. Johansson, K. Kulyk, S. Rosén, P. Rousseau, K. Støchkel, H. T. Schmidt, and H. Cederquist, *Nonstatistical Fragmentation of Large Molecules*, Phys. Rev. A **89**, 032701 (2014).

[12] J. A. Noble, C. Aupetit, D. Descamps, S. Petit, A. Simon, J. Mascetti, N. Ben Amor, and V. Blanchet, *Ultrafast Electronic Relaxations from the S_3 State of Pyrene*, Phys. Chem. Chem. Phys. **21**, 14111 (2019).

[13] F. Lépine, M. Y. Ivanov, and M. J. J. Vrakking, *Attosecond Molecular Dynamics: Fact or Fiction?*, Nat. Photonics **8**, 195 (2014).

[14] L. Belshaw, F. Calegari, M. J. Duffy, A. Trabattoni, L. Poletto, M. Nisoli, and J. B. Greenwood, *Observation of Ultrafast Charge Migration in an Amino Acid*, J. Phys. Chem. Lett. **3**, 3751 (2012).

[15] A. Marciniak, K. Yamazaki, S. Maeda, M. Reduzzi, V. Despré, M. Hervé, M. Meziane, T. A. Niehaus, V. Loriot, A. I. Kuleff, B. Schindler, I. Compagnon, G. Sansone, and F. Lépine, *Ultrafast Nonadiabatic Cascade and Subsequent Photofragmentation of Extreme Ultraviolet Excited Caffeine Molecule*, J. Phys. Chem. Lett. **9**, 6927 (2018).

[16] M. Lara-Astiaso, M. Galli, A. Trabattoni, A. Palacios, D. Ayuso, F. Frassetto, L. Poletto, S. De Camillis, J. Greenwood, P. Decleva, I. Tavernelli, F. Calegari, M. Nisoli, and F. Martín, *Attosecond Pump–Probe Spectroscopy of Charge Dynamics in Tryptophan*, J. Phys. Chem. Lett. **9**, 4570 (2018).

[17] A. Marciniak, V. Despré, T. Barillot, A. Rouzée, M. C. E. Galbraith, J. Klei, C.-H. Yang, C. T. L. Smeenk, V. Loriot, S. N. Reddy, A. G. G. M. Tielens, S. Mahapatra, A. I. Kuleff, M. J. J. Vrakking, and F. Lépine, *XUV Excitation Followed by Ultrafast Non-Adiabatic Relaxation in PAH Molecules as a Femto-Astrochemistry Experiment*, Nat. Commun. **6**, 7909 (2015).

[18] A. Marciniak, V. Despré, V. Loriot, G. Karras, M. Hervé, L. Quintard, F. Catoire, C. Joblin, E. Constant, A. I. Kuleff, and F. Lépine, *Electron Correlation Driven Non-Adiabatic Relaxation in Molecules Excited by an Ultrashort Extreme Ultraviolet Pulse*, Nat. Commun. **10**, 337 (2019).

[19] M. Hervé, V. Despré, C. P. Nash, V. Loriot, A. Boyer, A. Scognamiglio, G. Karras, R. Brédy, E. Constant, A. G. G. M. Tielens, A. I. Kuleff, and F. Lépine, *Ultrafast Dynamics of Correlation Bands Following XUV Molecular Photoionization*, Nat. Phys. **17**, 327 (2021).

[20] M. S. Deleuze and L. S. Cederbaum, *Formation of Satellite Bands in the Ionization Spectra of Extended Systems*, Phys. Rev. B **53**, 13326 (1996).

[21] See Supplemental Material at http://link.aps.org/supplemental/10.1103/PhysRevX.11.041012 for experimental set-up, data analysis, and complementary experimental results.

[22] S. P. Ekern, A. G. Marshall, J. Szczepanski, and M. Vala, *Photodissociation of Gas-Phase Polycyclic Aromatic Hydrocarbon Cations*, J. Phys. Chem. A **102**, 3498 (1998).

[23] B. West, S. R. Castillo, A. Sit, S. Mohamad, B. Lowe, C. Joblin, A. Bodi, and P. M. Mayer, *Unimolecular Reaction Energies for Polycyclic Aromatic Hydrocarbon ions*, Phys. Chem. Chem. Phys. **20**, 7195 (2018).

[24] H. W. Jochims, E. Ruhl, H. Baumgartel, S. Tobita, and S. Leach, *Size Effects on Dissociation Rates of Polycyclic Aromatic Hydrocarbon Cations: Laboratory Studies and Astrophysical Implications*, Astrophys. J. **420**, 307 (1994).

[25] A. Simon, M. Rapacioli, G. Rouaut, G. Trinquier, and F. X. Gadéa, *Dissociation of Polycyclic Aromatic Hydrocarbons: Molecular Dynamics Studies*, Phil. Trans. R. Soc. A **375**, 20160195 (2017).

[26] N. Bloembergen and A. H. Zewail, *Energy Redistribution In Isolated Molecules and the Question of Mode-Selective Laser Chemistry Revisited*, J. Phys. Chem. **88**, 5459 (1984).

[27] S. M. Beck, J. B. Hopkins, D. E. Powers, and R. E. Smalley, *Jet-Cooled Naphthalene. II. Single Vibronic Level Fluorescence Spectra*, J. Chem. Phys. **74**, 43 (1981).

[28] M. Vacher, M. J. Bearpark, M. A. Robb, and J. P. Malhado, *Electron Dynamics upon Ionization of Polyatomic Molecules: Coupling to Quantum Nuclear Motion and Decoherence*, Phys. Rev. Lett. **118**, 083001 (2017).

[29] F. Calegari, D. Ayuso, A. Trabattoni, L. Belshaw, S. De Camillis, S. Anumula, F. Frassetto, L. Poletto, A. Palacios, P. Decleva, J. B. Greenwood, F. Martin, and M. Nisoli, *Ultrafast electron Dynamics in Phenylalanine Initiated by Attosecond Pulses*, Science **346**, 336 (2014).

[30] B. J. West, L. Lesniak, and P. M. Mayer, *Why Do Large Ionized Polycyclic Aromatic Hydrocarbons Not Lose C_2H_2?*, J. Phys. Chem. A **123**, 3569 (2019).

[31] A. Eppink and D. Parker, *Velocity Map Imaging of Ions and Electrons Using Electrostatic Lenses: Application in Photoelectron and Photofragment Ion Imaging of Molecular Oxygen*, Rev. Sci. Instrum. **68**, 3477 (1997).